


Original Article

Automated SEM Image Analysis of the Sphere Diameter, Sphere-Sphere Separation, and Opening Size Distributions of Nanosphere Lithography Masks

Thomas Riedl*  and Jörg K.N. Lindner

Department of Physics and Center for Optoelectronics and Photonics Paderborn (CeOPP), Paderborn University, Warburger Straße 100, 33098 Paderborn, Germany

Abstract

Colloidal nanosphere monolayers—used as a lithography mask for site-controlled material deposition or removal—offer the possibility of cost-effective patterning of large surface areas. In the present study, an automated analysis of scanning electron microscopy (SEM) images is described, which enables the recognition of the individual nanospheres in densely packed monolayers in order to perform a statistical quantification of the sphere size, mask opening size, and sphere-sphere separation distributions. Search algorithms based on Fourier transformation, cross-correlation, multiple-angle intensity profiling, and sphere edge point detection techniques allow for a sphere detection efficiency of at least 99.8%, even in the case of considerable sphere size variations. While the sphere positions and diameters are determined by fitting circles to the spheres edge points, the openings between sphere triples are detected by intensity thresholding. For the analyzed polystyrene sphere monolayers with sphere sizes between 220 and 600 nm and a diameter spread of around 3% coefficients of variation of 6.8–8.1% for the opening size are found. By correlating the mentioned size distributions, it is shown that, in this case, the dominant contribution to the opening size variation stems from nanometer-scale positional variations of the spheres.

Key words: close-packed monolayers, nanosphere lithography, numerical image analysis, polystyrene colloids, scanning electron microscopy, size distribution

(Received 29 July 2021; revised 29 October 2021; accepted 5 December 2021)

Introduction

Nanosphere lithography (NSL) provides a cost-effective method to fabricate periodic nanopatterns on large surface areas (Hulteen & Van Duyne, 1995; Boneberg et al., 1997; Haginoya et al., 1997; Burmeister et al., 1999). Regular arrays have a great potential for applications, for example, in optoelectronics (Sim et al., 2011; Zhang et al., 2013), electrochemical sensors (Purwidyantri et al., 2016), optical fiber tip nanopropes (Pisco et al., 2017), and as metamaterials (Gwinner et al., 2009). Recently, it has been demonstrated that NSL masks can be fabricated in roll-to-roll processes, opening the path to industrial scale applications (Chen et al., 2020). Often, a narrow size distribution of the nanoobjects is desired in order to realize devices with well-defined emission or absorption properties (Haynes & Van Duyne, 2001; Qian et al., 2008). Therefore, it is important to determine the factors governing the size distribution of the nanoscale openings in the sphere monolayers or double layers, which serve as lithographic masks. In case of close-packed monolayer masks, the mask openings, also referred to as interstices, are defined by sphere triples.

Up to now, the mask opening size distribution has been investigated only indirectly by analyzing atomic force microscopy or scanning electron microscopy (SEM) images of nanoparticle arrays fabricated by physical vapor deposition through sphere layer masks (Hulteen & Van Duyne, 1995; Hulteen et al., 1999; Li & Zinke-Allmang, 2002; Riedl & Lindner, 2014). Li & Zinke-Allmang found that the size distribution of Ge particles deposited at the interstices of a polystyrene sphere monolayer is broader than that of the spheres, and ascribed the difference to packing imperfections of the spheres (Li & Zinke-Allmang, 2002). Hulteen et al. studied the size distributions of Ag nanoparticles obtained at the openings of polystyrene sphere mono- and double layers (Hulteen et al., 1999). The authors conclude that the standard deviation of the interstice size roughly equals that of the sphere diameter. However, if the sphere size variation was the only cause for the interstice size distribution, the coefficient of variation (CV) of the interstice size would be given by the CV of the average sphere diameters of the groups of three spheres (i.e., sphere triples) defining an interstice. In other words, the standard deviation of the interstice size would be significantly smaller than that of the sphere diameter. The reasons for this are two-fold: First, since the average diameter of the spheres in a triple determines the interstice size as a first approximation, sphere diameter differences level out partially, that is, the standard deviation of the average diameters of the spheres in a triple is smaller than that of the sphere diameters by a factor of $3^{1/2}$.

*Corresponding author: Thomas Riedl, E-mail: thomas.riedl@uni-paderborn.de

Cite this article: Riedl T, Lindner JKN (2022) Automated SEM Image Analysis of the Sphere Diameter, Sphere-Sphere Separation, and Opening Size Distributions of Nanosphere Lithography Masks. *Microsc Microanal* 28, 185–195. doi:10.1017/S1431927621013866

© The Author(s), 2021. Published by Cambridge University Press on behalf of the Microscopy Society of America. This is an Open Access article, distributed under the terms of the Creative Commons Attribution licence (<http://creativecommons.org/licenses/by/4.0/>), which permits unrestricted re-use, distribution, and reproduction in any medium, provided the original work is properly cited.

Second, the sphere diameter D is linearly interrelated to the interstice equivalent diameter $D_{\text{eq, is}}$, that is, the diameter of a circle with the same area as the interstice area (see Supplementary Section 1.1):

$$D_{\text{eq, is}} = \left(\frac{3^{1/2}}{\pi} - \frac{1}{2} \right)^{1/2} \cdot D \approx 0.227 \cdot D, \quad (1)$$

with a proportionality factor < 1 .

Thus, the experimentally observed larger CV of the interstice size as compared to the CV of the average sphere diameters of the triples indicates that there must exist further sources of size broadening. To the best of our knowledge, a direct analysis of the mask opening size distribution and of its geometric origins such as the sphere diameter distribution, sphere position variations and interstice corner rounding/filling due to surface energy minimization or deposition of solutes from the sphere suspension has not yet been made.

To analyze the size of the mask openings together with that of the spheres forming them, the individual spheres and triples of them have to be identified in the image. In order to detect nearly spherical objects corresponding to circles in the image, several methods are reported in the literature: Circle Hough transformation and its variants (Duda & Hart, 1975; Scaramuzza et al., 2005), the random sample consensus algorithm (Göttinger, 2015), correlation-based template matching (Ceccarelli et al., 2001), marker-based watershed segmentation (Gostick, 2017), and region-based convolutional neuronal networks (Girshick et al., 2014). While these techniques have enabled a remarkable progress in the detection of spherical objects, they also exhibit shortcomings. In the case of high-resolution SEM images of sphere monolayers, the sphere objects are partly interconnected in a nearly regular array containing defects. Due to the concomitant image intensity variations, in addition to noise, this can complicate the complete capture of the sphere edges, and thus lower the accuracy of the analysis, as well as give rise to false negative and false positive detection events. In our contribution, we develop an automated analysis procedure based on intensity profiling and cross-correlation, which is capable of quantifying the sphere diameters, the sizes of sphere triple interstices and sphere positions. The method is applied to widely used monodisperse polystyrene sphere monolayer masks with sphere diameters between 220 and 600 nm. In particular, the correlation between the evaluated quantities is assessed, and the relative importance of the factors leading to the observed interstice size distribution widths is determined. This knowledge will help identifying the materials and conditions favorable for obtaining ultra-narrow mask opening and thus nanostructure size distributions.

Materials and Methods

The experimental procedure used consists of a cleaning and hydrophilization treatment of Si wafer pieces, followed by the deposition of polystyrene sphere monolayers and then imaging in a scanning electron microscope. Rectangular pieces (4 cm × 2 cm) were cut from a 4-inch n-doped Si (001) wafer. After cleaning the surface by rinsing with deionized H₂O and isopropyl alcohol, the wafer pieces were hydrophilized by an O₂/Ar plasma treatment (2 sccm O₂, 8 sccm Ar, pressure 10 Pa, RF power 50 W, duration 3 min) in a Plasmalab 80plus machine (Oxford Instruments). The hydrophilicity was checked by means of optical measurements of the contact angle of deionized H₂O droplets

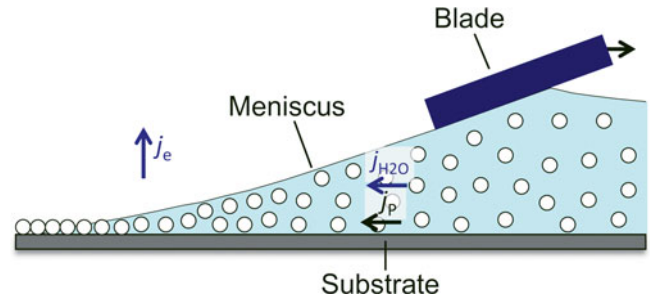


Fig. 1. Schematic cross-section view of the formation of colloidal monolayers at the three-phase contact line in the doctor blade technique. $j_{\text{H}_2\text{O}}$, j_p , and j_e denote the liquid H₂O, solid sphere particle, and H₂O evaporation fluxes.

placed on the wafer surface using a Drop Shape Analyzer DSA25E (Krüss company).

Next, monolayers of monodisperse polystyrene spheres with three different sphere sizes, 220, 370, and 600 nm were deposited from aqueous suspensions (10 wt% solids, Thermo Fisher Scientific Inc.) on the hydrophilized Si substrate by means of the doctor blade technique (Kumnorkaew et al., 2008; Riedl & Lindner, 2014). A drop of the colloidal suspension is pipetted onto the substrate surface, brought into contact with a blade and then moved at a constant velocity across the surface (Fig. 1). At the three-phase contact line between the substrate, the suspension and the gas atmosphere two-dimensional close-packed sphere layers form due to the action of attractive capillary forces between the spheres and the convective stream of suspension toward the three-phase line (Dimitrov et al., 1994; Kumnorkaew et al., 2008). In order to obtain sphere monolayers a suitable blade velocity was chosen, which depends on sphere size, temperature, and atmosphere humidity. The resulting sphere layers were imaged in a field emission SEM electron beam lithography system (Raith Pioneer) at 5 kV using an inlens detector.

Image Analysis Method

In this section, the individual image processing and evaluation steps are described. All steps are implemented in a script developed for the Gatan DigitalMicrograph software (GMS 2, 2014). The script is available in the DigitalMicrograph Script Database hosted by FELMI, Graz University of Technology (FELMI, 2021). As input data, unprocessed SEM images of sphere monolayers are used, which should have (i) sufficient spatial resolution and pixel density in order to clearly resolve the sphere outlines, (ii) a sufficient signal-to-noise ratio, and (iii) sufficient contrast between the spheres and their interstices. Recommended values

Table 1. Quality Parameters of SEM Images of Sphere Monolayers Recommended for the Automated Analysis.

Spatial Resolution (minimum resolvable distance)	Linear Pixel Density	Signal-to-Noise Ratio ^a	Average Contrast ^{b,c}
$\leq 2.5\%$ of D	$\geq 100/D$	≥ 7.5	≥ 0.3

^aSignal = intensity difference between the interstice and adjacent sphere interiors.

^bContrast = intensity difference between the interstice and adjacent sphere interiors divided by the mean intensity of the same interstice and sphere interiors.

^cAveraged over the entire image.

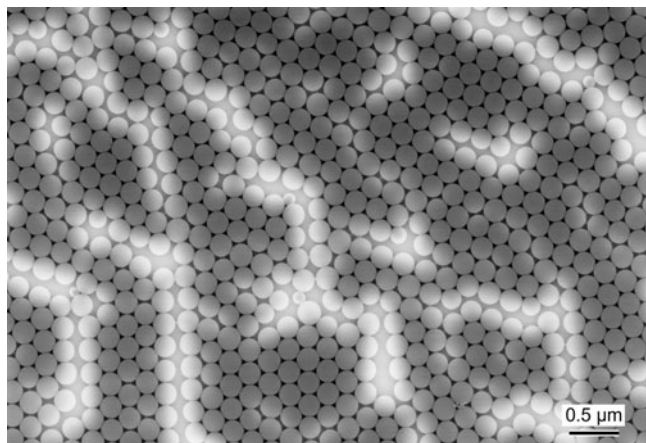


Fig. 2. Raw SEM image of a sphere monolayer showing more than 500 spheres with an average diameter of 220 nm.

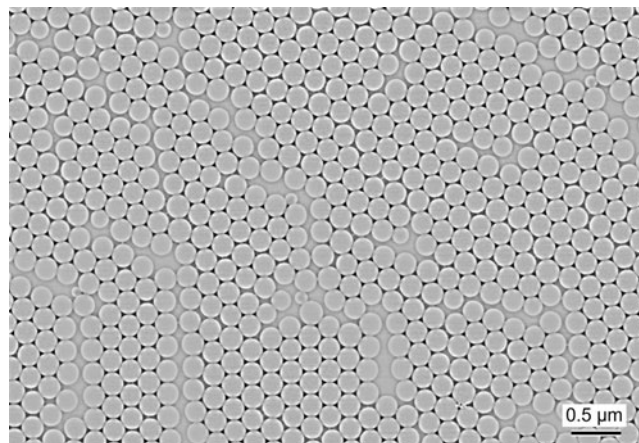


Fig. 3. Smooth-filtered and average-corrected version of the SEM image in Figure 2.

are listed in Table 1. For statistical analyses, the image area should cover several hundreds of spheres. The typical image size is 2,000 to 3,000 pixels in each dimension. An example of such an SEM image of a particularly defective sphere monolayer is given in Figure 2. Numerous line defects in the sphere arrangement and various mask defects involving overly small spheres are visible. Line defects appear brighter in the image since the spheres bordering the line charge up electrically, leading to a locally enhanced secondary electron emission. This example is chosen to demonstrate the robustness of the image analysis method developed in the following section.

Filtering and Average Correction

At the beginning of image analysis, two preparatory steps are performed. First, in order to minimize noise, the raw image is smooth-filtered by convolution in real space using a filter kernel. Each pixel is replaced by a weighted sum of its surrounding pixels. The array of weights for each of the surrounding pixels forms the kernel **K**. Here, the kernel

$$\mathbf{K} = \begin{matrix} 1 & 2 & 1 \\ 2 & 4 & 2 \\ 1 & 2 & 1 \end{matrix} \quad (2)$$

implemented in the “smooth” menu command of the DigitalMicrograph software is used. In this kernel, the center pixel has fourfold weight, whereas the central top, bottom, left, and right pixels have double, and the corner pixels single weight.

Second, a local average-corrected image $I_{\text{corr}}(x, y)$ is computed from the smooth-filtered image $I_{\text{sm}}(x, y)$, in order to reduce large-scale intensity variations due to differences in the secondary electron emission rate between the perfect crystalline areas and the zones containing defects:

$$I_{\text{corr}}(x, y) = \frac{I_{\text{sm}}(x, y)}{I_{\text{avg}}(x, y)} \cdot \bar{I}. \quad (3)$$

\bar{I} denotes the mean image intensity in the entire image and

$$I_{\text{avg}}(x, y) = \frac{\sum_{y'=y-b/2}^{y+b/2} \sum_{x'=x-b/2}^{x+b/2} I_{\text{sm}}(x', y')}{b^2} \quad (4)$$

the local average intensity image, which is obtained by assigning to each pixel (x, y) the average intensity of a square region of interest (ROI) of size b (with $b = \text{even integer}$ and $b \approx 40\%$ of the average sphere diameter) centered at (x, y) . The loop variables x', y' are confined inside the image boundaries. Figure 3 depicts the average-corrected image of the SEM image in Figure 2.

Taking the local average-corrected image as input, the sphere detection is achieved in three steps. In step 1, seed spheres are detected (20–30% of all spheres), followed by the detection of the large majority of spheres in step 2 and a search optimized for spheres of deviating size in step 3. All three steps include fitting circles to the sphere circumferences.

Seed Sphere Detection

Seed sphere detection starts with the preselection of possible sphere positions by defining a grid of square ROIs (ROI size: 1.3 times the sphere diameter D) on the image. Each ROI is then cross-correlated with an equally sized reference image of a fully six-fold coordinated sphere, which is taken from the image at a position specified by the user. If the distance between the detected position of the correlation maximum and the ROI center is below a threshold value of $D/3$ (determined from test runs), an ROI of the same size centered at the correlation maximum is examined by means of an intensity profiling module. This module extracts intensity profiles along lines inclined by various angles centered at the correlation maximum position (Figs. 4a, 4b). Typically, 18 profiles are extracted using equidistant angular steps. In order to minimize the intensity scatter, the profiles have a width of a few pixels (not shown in Fig. 4a). Next, intensity steps with sufficient height and not too large width are searched in these profiles in order to determine the edges of the sphere. If these intensity steps (i) either have positive sign and are situated in the first profile half, or have negative sign and occur in the second profile half, and if (ii) the distance between two such steps of

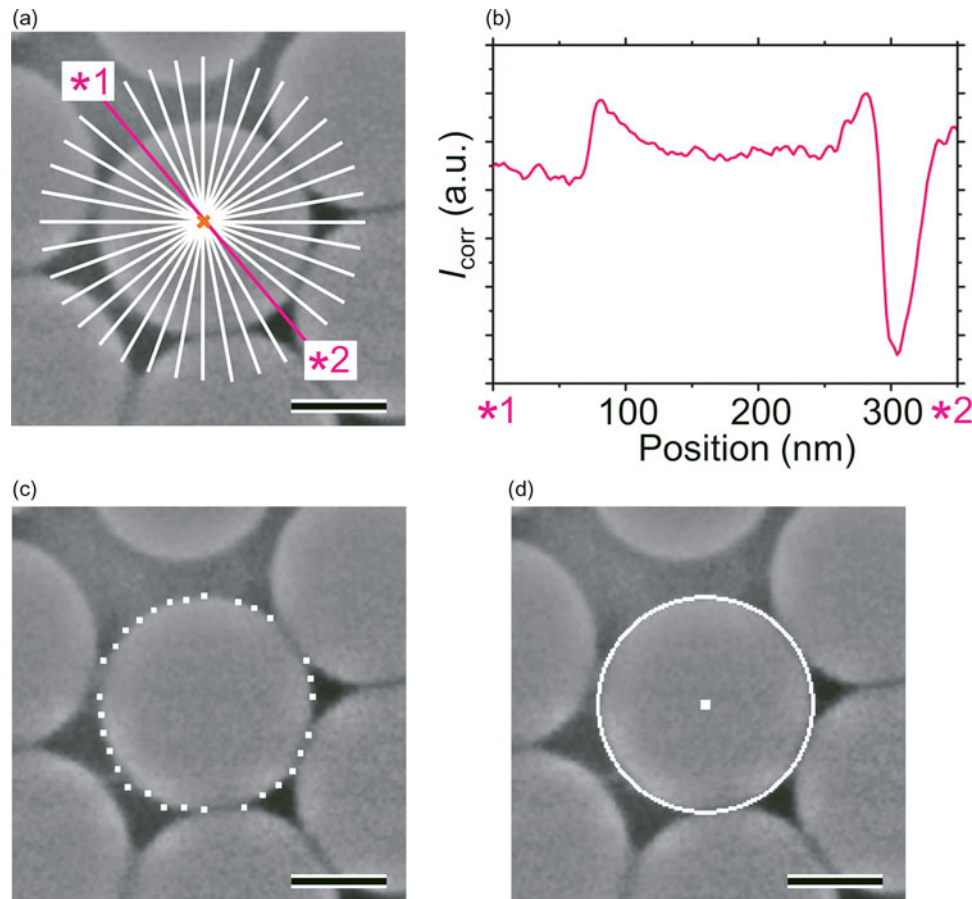


Fig. 4. (a) Enlarged subarea of the SEM image of Figure 3 with a marked example position and the corresponding 18 intensity profile lines, (b) the intensity profile marked by a star in (a), (c,d) same image subarea as in (a) with (c) marked sphere edge points and (d) fitted circle line and center position. The length bar is 100 nm in (a,c,d).

opposite sign lies within the interval

$$\text{Intvl} = [(1 - k_1)\bar{D}; (1 + k_2)\bar{D}], \quad (5)$$

with $k_1 = k_2 = 0.2$ and \bar{D} is an approximate estimate of the average sphere diameter (input by the user), then the step positions are recognized as points on the sphere circumference, that is, sphere edge points (Fig. 4c). The restriction for the separation of two steps of opposite sign helps to minimize the detection of false positions. If more than a user-defined number of edge points (typically 16 for 18 profiles) are found, a circle is fitted to them by means of an iterative procedure (Fig. 4d). In case of a sufficiently high fit quality (measured as the sum of squared distances between circle and edge points, normalized to the number of points), the fitted position is accepted as a sphere center position. Figure 5 depicts the SEM image with all 133 detected seed spheres marked.

Sphere Detection Step 2

In contrast to the raster search for the seed spheres, the detection algorithms used in step 2 to find the large majority of spheres rely on combined star and 360° searches. The star search works most effectively in case of perfect monocrystalline sphere arrangements. The name of this search reflects the six different search directions along the close-packed directions in the 2D lattice starting out from the seed sphere positions. For the determination of these

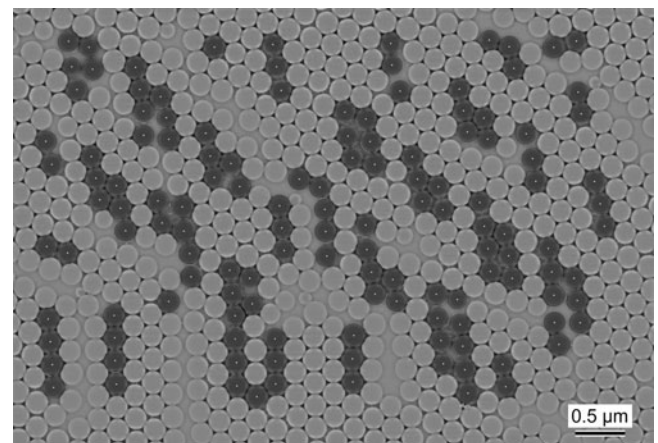


Fig. 5. SEM image of Figure 3 with 133 fitted seed spheres. The fitted spheres are highlighted as dark grey areas with the center positions marked as white dots.

directions, the angular positions of the maxima in the Fourier transforms of ROIs are evaluated, where the ROIs are centered at the positions of the seed spheres (Figs. 6a, 6b). In this way, new potential sphere positions in the first nearest-neighbor shell are identified at a distance to the seed sphere that equals the estimated average sphere diameter. In addition, further 54 potential positions are identified in the second, third, and fourth nearest-

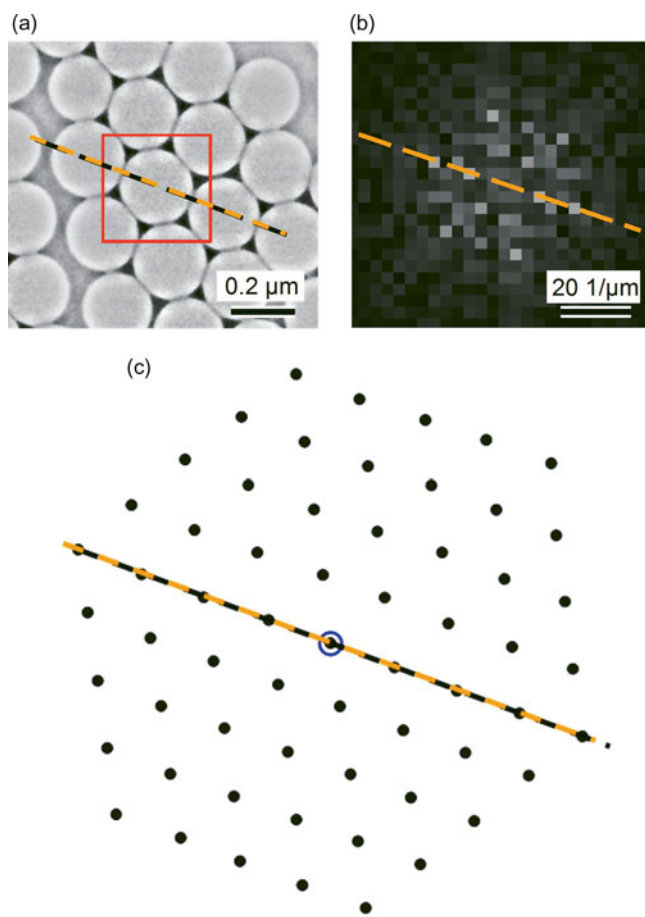


Fig. 6. Star sphere search: (a) subarea of the SEM image of Figure 3; the square marks the area used for the Fourier transformation. (b) Central part of the Fourier transform magnitude image computed from the marked area in (a). In (a), (b) and (c), the close-packed direction is highlighted that belongs to the most-intense off-center Fourier peak. For the purpose of finding this peak, the central Fourier maximum has been removed. (c) Detected lattice positions corresponding to the sphere arrangement of (a), which are proposed as potential sphere positions. The seed sphere is marked with a small blue circle.

neighbor shells by assuming the spheres to sit on regular positions of the close-packed 2D lattice (Fig. 6c). Analogously to the seed sphere detection procedure, the positions are refined by means of cross-correlation, then subjected to the intensity profiling (see Section “Seed sphere detection”), sphere edge point detection and fitting routines described above. As the star search assumes a perfect lattice, it often does not recognize spheres located at defects occurring in the sphere monolayers, namely small gaps between neighboring spheres, line defects and small zones with reduced sphere coordination. Therefore, a 360° search has been developed, which is suitable for disordered sphere arrangements with 1–6 nearest neighbors. Here, the cross-correlation between the reference sphere image and image ROIs centered at a fixed distance (estimated sphere diameter) from the seed sphere center is evaluated as a function of the azimuth angle (Figs. 7a, 7b). The positions with maximum correlation are then selected for the subsequent intensity profiling, edge point, and fitting operations, as described above. In order to include positions further away from the seed sphere, the 360° search has been programmed as an endless routine, that is, it is repeated taking the newly detected position as starting position. The process continues as long as further not yet detected nearest-neighbor spheres are recognized inside the image

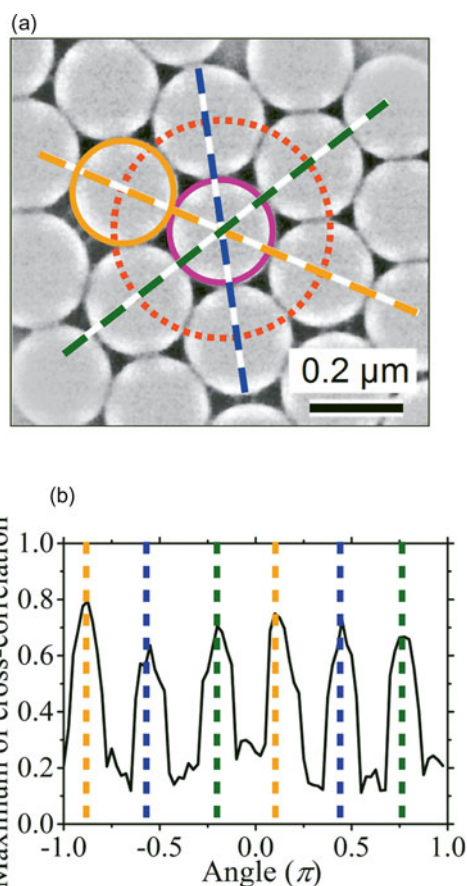


Fig. 7. 360° sphere search: (a) subarea of the SEM image of Figure 3; the central seed sphere and the nearest-neighbor sphere displaying the largest cross-correlation are marked in violet and orange, respectively. (b) Maximum values of the cross-correlation images plotted as a function of the azimuth angle. The cross-correlation images are computed from the reference sphere image and image ROIs positioned at variable azimuth angle at a constant distance to the seed sphere center (the red dotted circle line). In (a, and (b), the colored dashed lines mark the directions or angular positions that correspond to the cross-correlation maxima in plot (b).

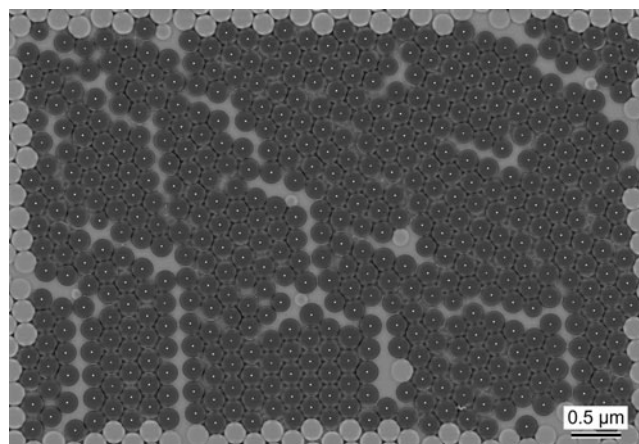


Fig. 8. SEM image of Figure 3 with 519 marked fitted spheres, which have been detected in course of the sphere searches of step 1 (seed spheres) and step 2 (combined star and 360° searches).

boundaries. As illustrated in Figure 8, the combined star and 360° searches are capable of detecting around 99% of the spheres (seed spheres included, image border regions excluded).

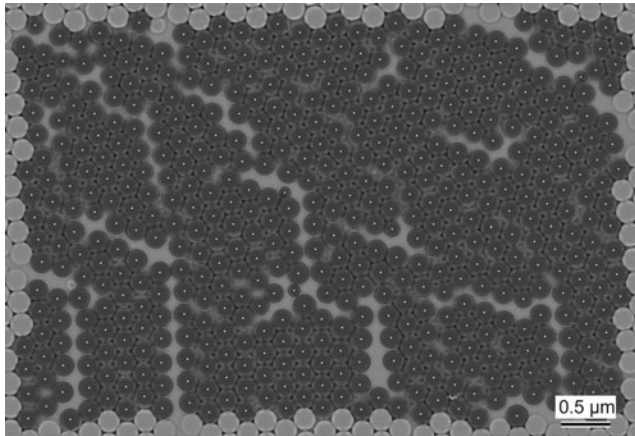


Fig. 9. SEM image of Figure 3 with 525 marked fitted spheres, which have been detected in course of the sphere searches of steps 1–3.

Detection of Spheres of Deviating Size

As the sphere search steps 1 and 2 are designed for average-sized spheres, spheres of deviating size, in the present case mostly significantly smaller spheres, are often overlooked. To include these spheres with diameters significantly below the average, a third search step is conducted. In this step, potential sphere positions outside the fitted circles of the before detected spheres are identified. These positions are examined by using intensity profiling and a modified sphere edge point detection routine which is opened for a wider range of sphere diameters by choosing appropriate values for k_1 and k_2 in equation (5). The fitting is performed as described in steps 1 and 2. Overall, at least 99.8% of all spheres are detected (image border regions excluded), and accurate fit results for their center positions and diameters obtained (Fig. 9). Based on these data, the sphere diameter histogram and statistical key figures such as average, standard deviation, and CV are evaluated.

Identification of Sphere Triples

Based on the analysis described before, another module of the program identifies the sphere triples as a preparatory step for the interstice size evaluation. By sphere triples we mean sets of three spheres, where each of the three spheres forms a contact to the other two spheres. The triple identification is performed by means of intensity profile analyses. For each two spheres with separation

$$s = \overline{M_1M_2} - R_1 - R_2 \quad (6)$$

($\overline{M_1M_2}$ is the distance between the sphere centers M_1, M_2 ; R_1, R_2 are fitted sphere radii) below a threshold value, the M_1M_2 center-to-center profile and the profile perpendicular to M_1M_2 through the radius weighted center point S_{12} of M_1M_2 are extracted (Fig. 10). The coordinates of point S_{12} are given by

$$\begin{pmatrix} x_{S_{12}} \\ y_{S_{12}} \end{pmatrix} = \frac{R_2}{R_1 + R_2} \begin{pmatrix} x_{M_1} \\ y_{M_1} \end{pmatrix} + \frac{R_1}{R_1 + R_2} \begin{pmatrix} x_{M_2} \\ y_{M_2} \end{pmatrix}. \quad (7)$$

On the one hand, in case of two spheres forming a contact to each other, the perpendicular profile displays a significant

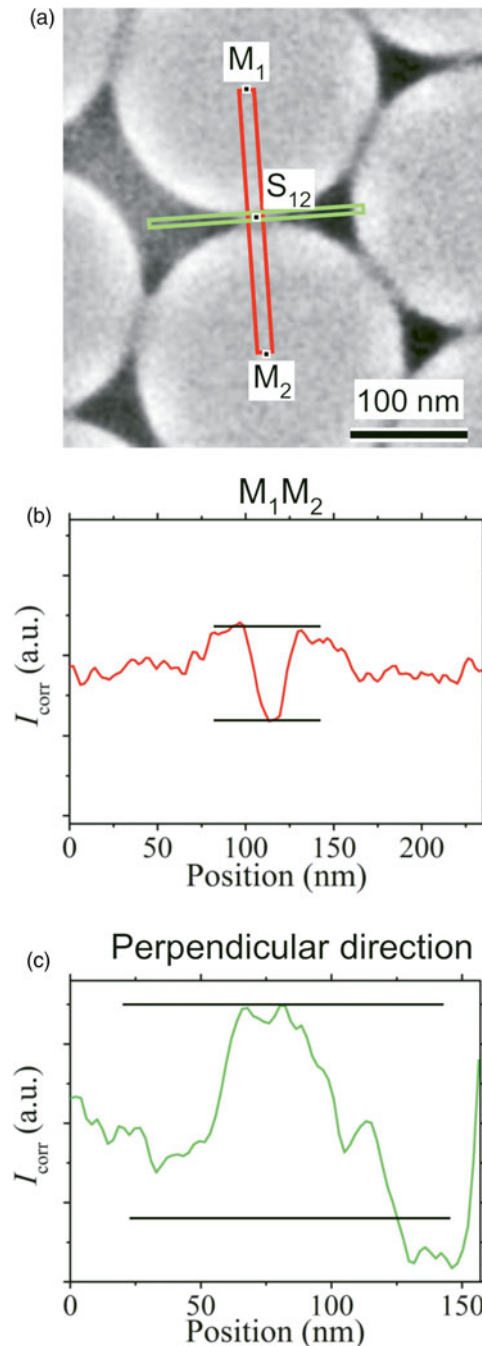


Fig. 10. Analysis performed for the recognition of sphere-sphere contact points. (a) Enlarged portion of the SEM sphere layer image of Figure 3, (b) and (c) intensity profiles extracted along the long sides of the rectangles marked in the SEM image. (b) Profile from sphere center to sphere center (M_1M_2) (red), (c) profile perpendicular to M_1M_2 through the radius weighted center point S_{12} (green). The vertical axes of the profiles cover intensity intervals of equal width. Horizontal line pairs mark the evaluated intensity differences (see text).

maximum in the vicinity of S_{12} , which separates two minima corresponding to the two adjacent interstices. On the other hand, if the two spheres do not touch each other, the M_1M_2 profile shows a pronounced minimum in the vicinity of S_{12} . Therefore, the two spheres are regarded to have a common contact, if the average intensity difference between the maximum and the two adjacent minima in the perpendicular profile exceeds a certain fraction

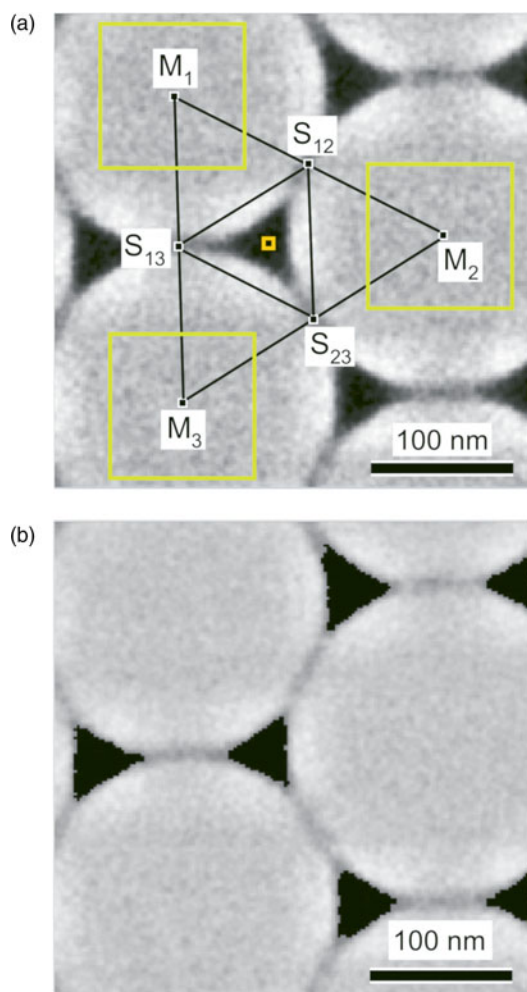


Fig. 11. (a) Subarea of the SEM image of Figure 3 showing a sphere triple and its central interstice. Marked are the sphere centers, the sphere-sphere contact points, as well as the regions in the spheres and in the interstice that are used for defining the intensity threshold for interstice quantification [equation (8)]. (b) Same SEM image subarea as (a) with thresholded interstice pixels marked in black.

f_{CP} of the depth of the intensity minimum in the M_1M_2 profile. The depth of this minimum is taken as the average intensity difference between the minimum and the adjacent two maxima. Both intensity differences are marked as horizontal lines in Figure 10. In agreement with the visual perception of contact points, $f_{CP} = 0.6$ has been chosen. Once the sphere pairs have been identified, the sphere triples are found by searching for sets composed of three sphere pairs that have three common spheres.

Interstice Quantification

After having identified the sphere triples, the corresponding interstice areas are quantified. For each triple i , an intensity threshold $I_{thres, i}$ is applied to the triangular region defined by the three sphere-sphere contact points S_{12} , S_{23} , and S_{13} (Fig. 11a):

$$I_{thres, i} = (1 - f) \cdot \langle I_{is\ center, i} \rangle + f \cdot \langle I_{triple\ spheres, i} \rangle. \quad (8)$$

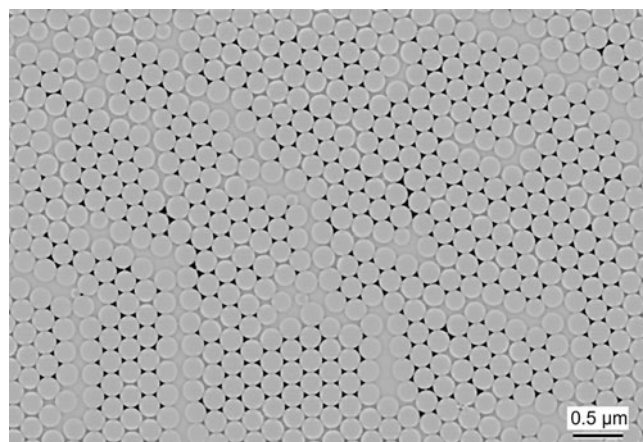


Fig. 12. SEM image of Figure 3 with 593 detected interstices marked in black.

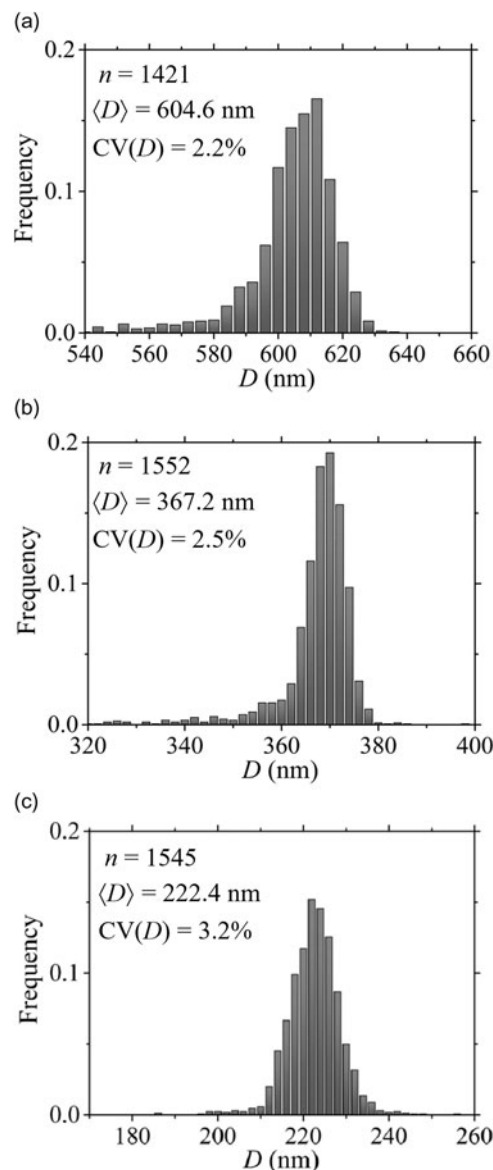


Fig. 13. Diameter histograms of the spheres involved in triples for different nominal sphere sizes: (a) 600 nm, (b) 370 nm, and (c) 220 nm. Also, the number of spheres n , the average diameter $\langle D \rangle$, and the diameter CV are given, respectively.

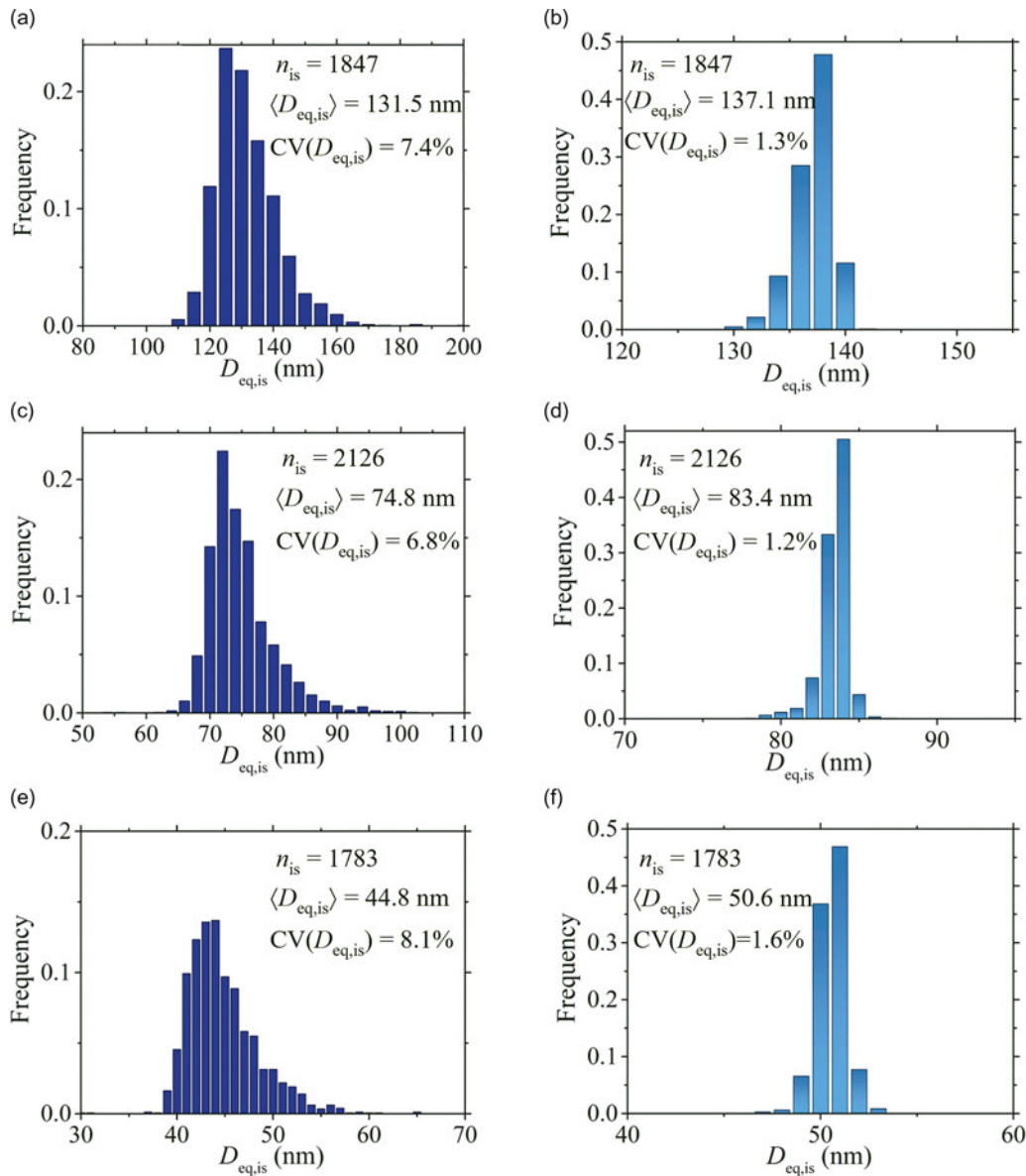


Fig. 14. Histograms of the interstice equivalent diameters for different nominal sphere sizes. **(a,b)** 600 nm, **(c,d)** 370 nm, and **(e,f)** 220 nm. **(a,c, e)** refer to the actually detected interstices; **(b,d,f)** relate to interstices if the spheres would be ideally spherical and would have contact points instead of contact areas or necks. The number of interstices n_{is} , the average interstice size $\langle D_{eq, is} \rangle$, and the CV are given, respectively.

$\langle I_{is \text{ center}, i} \rangle$ denotes the average intensity of a small region at the interstice center, and $\langle I_{\text{triple spheres}, i} \rangle$ denotes the average intensity in the center of the three spheres. The interstice center is approximated by the center of gravity of the triangle $\Delta S_{12}S_{23}S_{13}$. A threshold factor of $f = 0.5$ has been chosen so that the thresholded interstice region matches the visual perception of the interstice in the SEM image (Figs. 11a, 11b). Figure 12 displays the entire SEM image with all detected interstices marked in black.

Results and Discussion

Figures 13–15 display the sphere size, interstice size, and sphere-sphere separation histograms for nominal sphere diameters of 600, 370, and 220 nm, respectively. The quantified measure for the interstice size is the equivalent diameter $D_{eq, is}$, that is, the diameter of a circle having the same area as the interstice. For

each sphere size, SEM images covering more than 1,400 spheres were evaluated. It is found that the variations of the evaluated quantities with the macroscopic position in the sphere layer are small compared to their distribution widths, that is, the monolayers are homogeneous across the sample surface. The sphere diameter distribution is characterized by an approximately symmetric maximum with the average $\langle D \rangle$ being very close to the nominal sphere diameter specified by the supplier (Fig. 13). Remarkably, diameters significantly below the average occur more often than above-average diameters, owing to the sphere synthesis. Although all three sphere sizes have a CV value of $\leq 3\%$ specified by the supplier, the results show that the sphere diameter distribution width increases from 2.2 to 3.2% when decreasing the sphere size from 600 to 220 nm. For comparison, a manual evaluation of arbitrarily chosen subsets has been performed by tracing the outlines of around 50 spheres (part of sphere triples) and

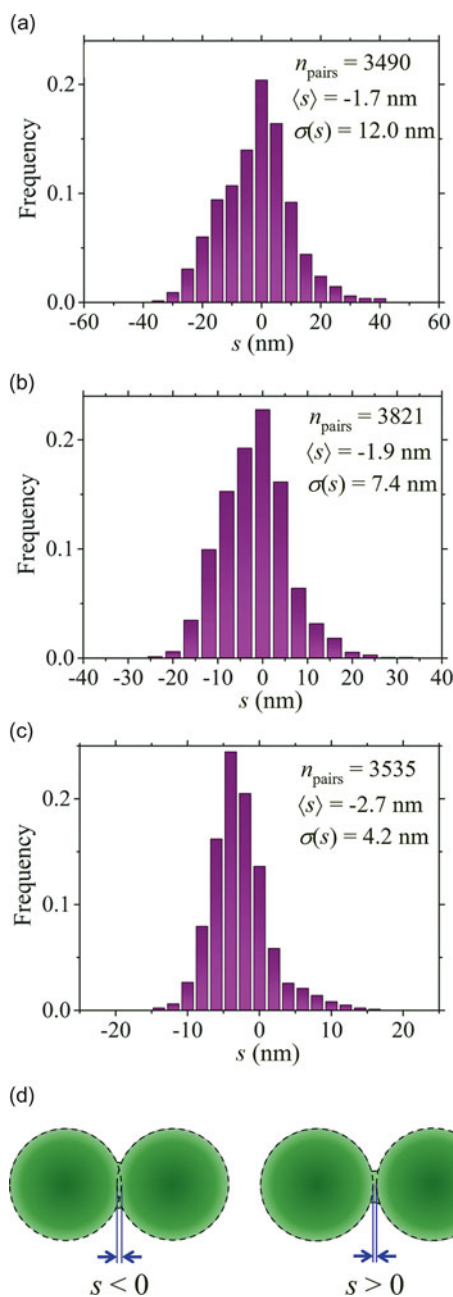


Fig. 15. (a–c) Histograms of the separations s between each two neighboring spheres in contact with each other for different nominal sphere sizes: (a) 600 nm, (b) 370 nm, and (c) 220 nm. The number of sphere pairs n_{pairs} , the average separation $\langle s \rangle$, and the standard deviation $\sigma(s)$ are given, respectively. (d) Schematics illustrating negative and positive separation s between the fit circles (dashed lines) of the two spheres.

counting the number of enclosed pixels. This yields CV values of 1.7 and 2.7%, while those of the program for the same subsets amount to 1.7 and 2.9%, respectively.

In contrast to the sphere diameter distributions, the interstice size histograms show a clear asymmetry with a pronounced tail on the above-average side (Figs. 14a, 14c, 14e). The interstice equivalent diameter CV values range between 6.8 and 8.1%, exhibiting no clear dependence on sphere size. A manual evaluation of arbitrarily chosen subsets comprising 50 interstices of the 600 and 220 nm sphere layers, respectively, gives CV values of 7.5 and 6.4%, as compared to 7.0 and 6.9% when applying the automatic

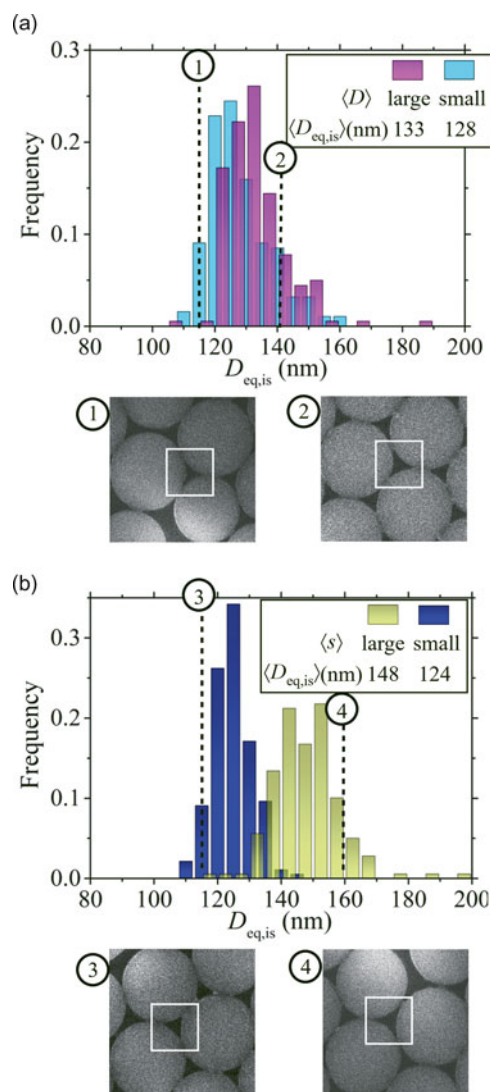


Fig. 16. Equivalent diameter histograms of interstice subsets for the 600 nm polystyrene sphere monolayer: (a) interstices with the large and small average diameter of the spheres in a triple, (b) interstices with the large and small average separation s of the spheres in a triple. “Large” and “small” refer to the 10% percentiles. Each histogram includes 185 interstices. To the right of each histogram, SEM image ROIs with example interstices illustrating the effects of sphere size and sphere-sphere separation are displayed. The encircled numbers 1 or 3 correspond to small sphere diameter or s , and 2 or 4 to large sphere diameter or s , marked in the histograms, respectively.

evaluation to the same subsets. Obviously, the interstice size CVs are larger by a factor of 2.5–3.4 than those of the sphere diameters. Figures 14b, 14d, and 14f depict the histograms of the sizes that the interstices would have if they were defined by ideal spheres having (i) contact points instead of contact areas or necks and (ii) the same diameter distributions as that of the detected spheres (for the calculation, see Supplementary Section 1.2). These ideal interstice size histograms display narrow, approximately symmetric distributions with CV values equal to around half the CV of the sphere size distributions, because of the levelling of sphere diameter variations in the triples. Moreover, the average actual interstice sizes amount to only 89–96% of the average ideal sizes, which can be explained by the presence of extended sphere-sphere contact zones leading to a shortening of the interstice corners.

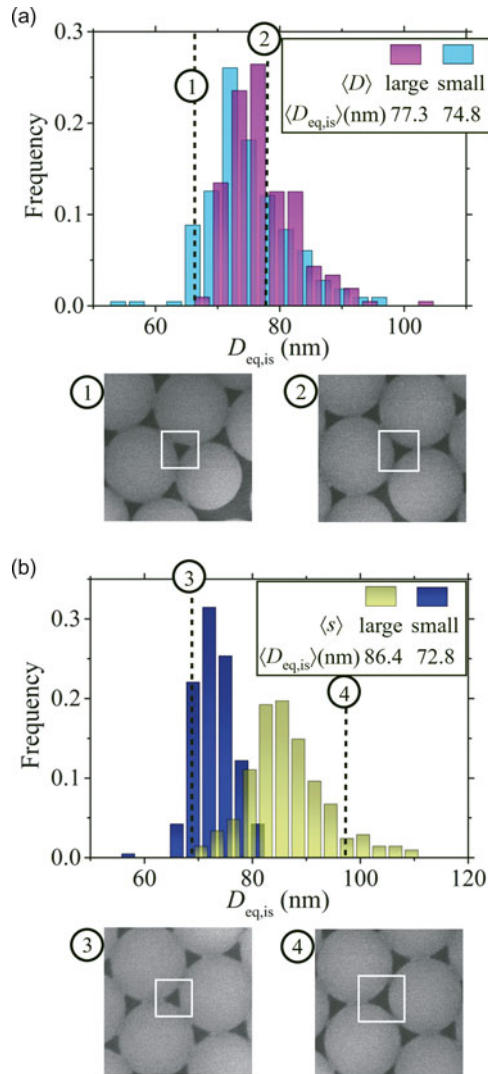


Fig. 17. Equivalent diameter histograms of interstice subsets for the 370 nm polystyrene sphere monolayer: (a) interstices with the large and small average diameter of the spheres in a triple, (b) interstices with the large and small average separation s of the spheres in a triple. “Large” and “small” refer to the 10% percentiles. Each histogram includes 212 interstices. To the right of each histogram, SEM image ROIs with example interstices illustrating the effects of sphere size and sphere-sphere separation are displayed. The encircled numbers 1 or 3 correspond to small sphere diameter or s , and 2 or 4 to large sphere diameter or s , marked in the histograms, respectively.

The discrepancy between the actual and the ideal interstice size distribution widths can be ascribed to small positional variations of the spheres in conjunction with the formation of contact necks between adjacent spheres as well as sphere deformations. As shown in Figures 15a and 15c, the separation s [equation (6)] between the circles fitted to the outlines of touching spheres ranges from around -6 to $+6\%$ of the sphere diameter. In case of negative s , the spheres are flattened along the contact zone, whereas the spheres are connected via small necks or bridges in case of positive s (Fig. 15d). These morphologies may arise as a consequence of collisions between the viscoelastic polymer spheres as well as condensation of styrene units from the liquid phase during the convective sphere layer self-assembly. Moreover, attractive van der Waals forces act between polystyrene

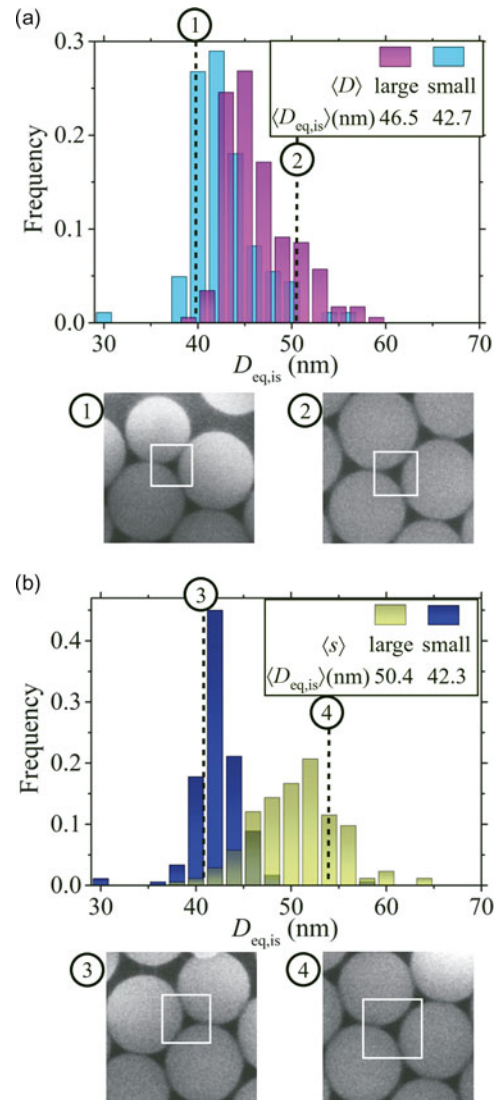


Fig. 18. Equivalent diameter histograms of interstice subsets for the 220 nm polystyrene sphere monolayer: (a) interstices with the large and small average diameter of the spheres in a triple, (b) interstices with the large and small average separation s of the spheres in a triple. “Large” and “small” refer to the 10% percentiles. Each histogram includes 178 interstices. To the right of each histogram, SEM image ROIs with example interstices illustrating the effects of sphere size and sphere-sphere separation are displayed. The encircled numbers 1 or 3 correspond to small sphere diameter or s , and 2 or 4 to large sphere diameter or s , marked in the histograms, respectively.

chains on opposing sphere surfaces leading to a reduction of surface area.

In order to analyze the influence of the sphere diameters on the interstice sizes, the interstice equivalent diameter distributions are plotted for the 10% largest and the 10% smallest average sphere diameters, respectively (Figs. 16a, 17a, 18a). The average diameter refers here to the spheres in a triple forming a mask opening. The histograms for large and small spheres largely overlap, where the average size of interstices $\langle D_{eq, is} \rangle$ formed by large spheres exceeds that of the small spheres by 4.3% for 600 nm spheres, 3.3% for 370 nm spheres, and 8.9% for 220 nm spheres. A more pronounced difference is found for the interstice equivalent diameters formed by spheres having the 10% largest and smallest sphere-sphere separations s (Figs. 16b, 17b, 18b): For

all sphere sizes, the average interstice diameter in case of large s is 19% larger than that for small s . Therefore, the position variations of the spheres in a triple constitute a major contribution to the interstice size distribution width for the analyzed sphere layers. However, this might not necessarily hold for other sphere suspensions and/or sphere layer deposition conditions, since the extent of position variations is expected to depend on the interplay between the self-assembly dynamics and the properties of the solid sphere and substrate materials as well as of the liquid phase. An investigation of these factors is beyond the scope of the present study and subject of further research.

Conclusion

In summary, a program for the automatic analysis of sphere diameters, interstice sizes, and sphere-sphere separations from SEM images of sphere monolayer masks has been devised. The program also enables a correlated analysis of these quantities, that is, the evaluation of interstice size distributions as a function of sphere size and sphere-sphere separation. This analysis has been applied to polystyrene sphere monolayers with sphere diameters in the range between 220 and 600 nm. For all sphere sizes, interstice equivalent diameter CV values of 6.8–8.1% have been determined, which are significantly larger than the diameter CV values of the spheres in a triple of 2.2–3.2%. As a result, the largest contribution to these observed spreads of interstice sizes stems from the spread of the sphere-sphere contact areas, which is closely related to positional variations of the spheres in a triple. In conjunction with the convective sphere layer self-assembly, the polymeric nature of the sphere material and related viscoelastic behavior as well as residual monomers in the colloidal liquid condensing at the sphere contacts lead to the formation of sphere-sphere contact zones as well as necks of variable dimension. In order to minimize the spread of interstice sizes, non-viscous inorganic spheres with low deformability such as SiO₂ could be used.

Supplementary material. To view supplementary material for this article, please visit <https://doi.org/10.1017/S1431927621013866>.

Acknowledgments. The authors would like to thank D. Drude, M. Kismann, and K.-U. Uhe for deposition of the sphere layers. Furthermore, we are grateful to Deutsche Forschungsgemeinschaft for financial support under Grants No. RI 2655/1-1 and No. LI 449/16-1.

Competing Interests. The authors declare that they have no competing interest.

References

- Boneberg J, Burmeister F, Schäfle C & Leiderer P (1997). The formation of nano-dot and nano-ring structures in colloidal monolayer lithography. *Langmuir* **13**, 7080–7084.
- Burmeister F, Badowsky W, Braun T, Wieprich S, Boneberg J & Leiderer P (1999). Colloid monolayer lithography – A flexible approach for nanostructuring of surfaces. *Appl Surf Sci* **144–145**, 461–466.
- Ceccarelli M, Petrosino A & Laccetti G (2001). Circle detection based on orientation matching. *Proceedings of the 11th International Conference on Image Analysis and Processing*, pp. 119–124.
- Chen I-T, Schappell E, Zhang X & Chang C-H (2020). Continuous roll-to-roll patterning of three-dimensional periodic nanostructures. *Microsyst Nanoeng* **6**, 22.
- Dimitrov AS, Dushkin CD, Yoshimura H & Nagayama K (1994). Observations of latex particle two-dimensional-crystal nucleation in wetting films on mercury, glass, and mica. *Langmuir* **10**, 432–440.
- Duda RO & Hart PE (1975). Use of the Hough transform to detect lines and curves in pictures. *Commun ACM* **18**, 509–517.
- FELMI (2021). DigitalMicrograph Script Database. Available at: www.felmi-zfe.at/dm-script (accessed July 15, 2021).
- Girshick R, Donahue J, Darrell T & Malik J (2014). Rich feature hierarchies for accurate object detection and semantic segmentation. *IEEE Conference on Computer Vision and Pattern Recognition*, pp. 580–587.
- GMS 2 (2014). Gatan Microscopy Software Suite. Available at: www.gatan.com/products/tem-analysis/gatan-microscopy-suite-software (accessed July 15, 2021).
- Gostick JT (2017). Versatile and efficient pore network extraction method using marker-based watershed segmentation. *Phys Rev E* **96**, 023307.
- Göttinger M (2015). Object detection and flight path prediction. Diploma thesis, Vienna University of Technology.
- Gwinner MC, Koroknay E, Fu L, Patoka P, Kandulski W, Giersig M & Giessen H (2009). Periodic large-area metallic split-ring resonator metamaterial fabrication based on shadow nanosphere lithography. *Small* **5**, 400–406.
- Haginoya C, Ishibashi M & Koike K (1997). Nanostructure array fabrication with a size-controllable natural lithography. *Appl Phys Lett* **71**, 2934–2936.
- Haynes CL & Van Duyne RP (2001). Nanosphere lithography: A versatile nanofabrication tool for studies of size-dependent nanoparticle optics. *J Phys Chem B* **105**, 5599–5611.
- Hulteen JC, Treichel DA, Smith MT, Duval ML, Jensen TR & Van Duyne RP (1999). Nanosphere lithography: Size-tunable silver nanoparticle and surface cluster arrays. *J Phys Chem B* **103**, 3854–3863.
- Hulteen JC & Van Duyne RP (1995). Nanosphere lithography: A materials general fabrication process for periodic particle array surfaces. *J Vac Sci Technol A* **13**, 1553–1558.
- Kumnorkaew P, Ee Y-K, Tansu N & Gilchrist JF (2008). Investigation of the deposition of microsphere monolayers for fabrication of microlens arrays. *Langmuir* **24**, 12150–12157.
- Li N & Zinke-Allmang M (2002). Size-tunable Ge nano-particle arrays patterned on Si substrates with nanosphere lithography and thermal annealing. *Jpn J Appl Phys* **41**, 4626–4629.
- Pisco M, Galeotti F, Quero G, Grisci G, Micco A, Mercaldo LV, Veneri PD, Cutolo A & Cusano A (2017). Nanosphere lithography for optical fiber tip nanopores. *Light Sci Appl* **6**, e16229.
- Purwidyantri A, Chen C-H, Hwang B-J, Luo J-D, Chiou C-C, Tian Y-C, Lin C-Y, Cheng C-H & Lai C-S (2016). Spin-coated Au-nanohole arrays engineered by nanosphere lithography for a *Staphylococcus aureus* 16S rRNA electrochemical sensor. *Biosens Bioelectron* **77**, 1086–1094.
- Qian X, Li J, Wasserman D & Goodhue WD (2008). Uniform InGaAs quantum dot arrays fabricated using nanosphere lithography. *Appl Phys Lett* **93**, 231907.
- Riedl T & Lindner JKN (2014). Self-organized fabrication of periodic arrays of vertical, ultra-thin nanopillars on GaAs surfaces. *Phys Status Solidi A* **211**, 2871–2877.
- Scaramuzza D, Pagnottelli S & Valigi P (2005). Ball detection and predictive ball following based on a stereoscopic vision system. *Proceedings of the IEEE International Conference on Robotics and Automation*, pp. 1561–1566.
- Sim JI, Lee BG, Yang JW, Yoon H & Kim TG (2011). The light extraction efficiency of p-GaN patterned InGaN/GaN light-emitting diodes fabricated by size-controllable nanosphere lithography. *Jpn J Appl Phys* **50**, 102101.
- Zhang L-C, Yang G, Wang K, Fu M, Wang Y, Long H & Lu P-X (2013). Highly ordered ZnO nanohole arrays: Fabrication and enhanced two-photon absorption. *Opt Commun* **291**, 395–399.